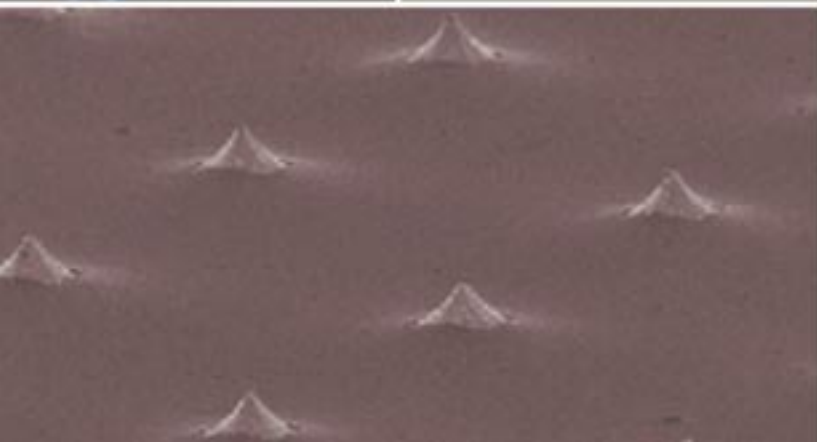
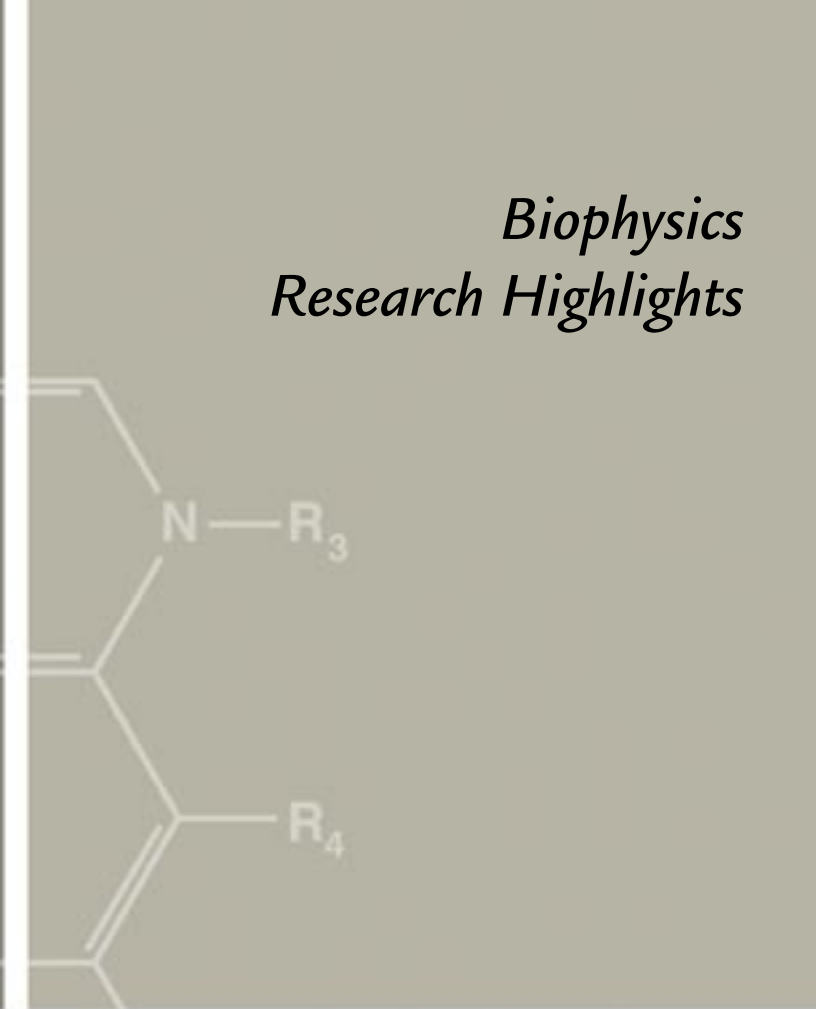
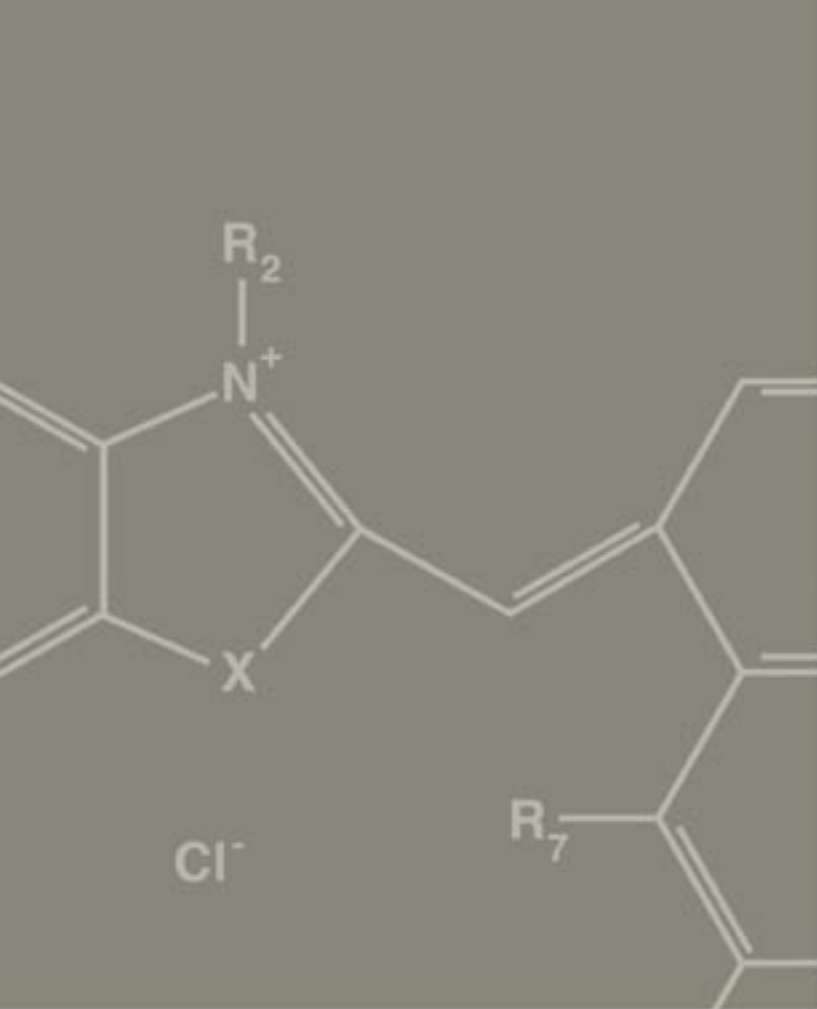
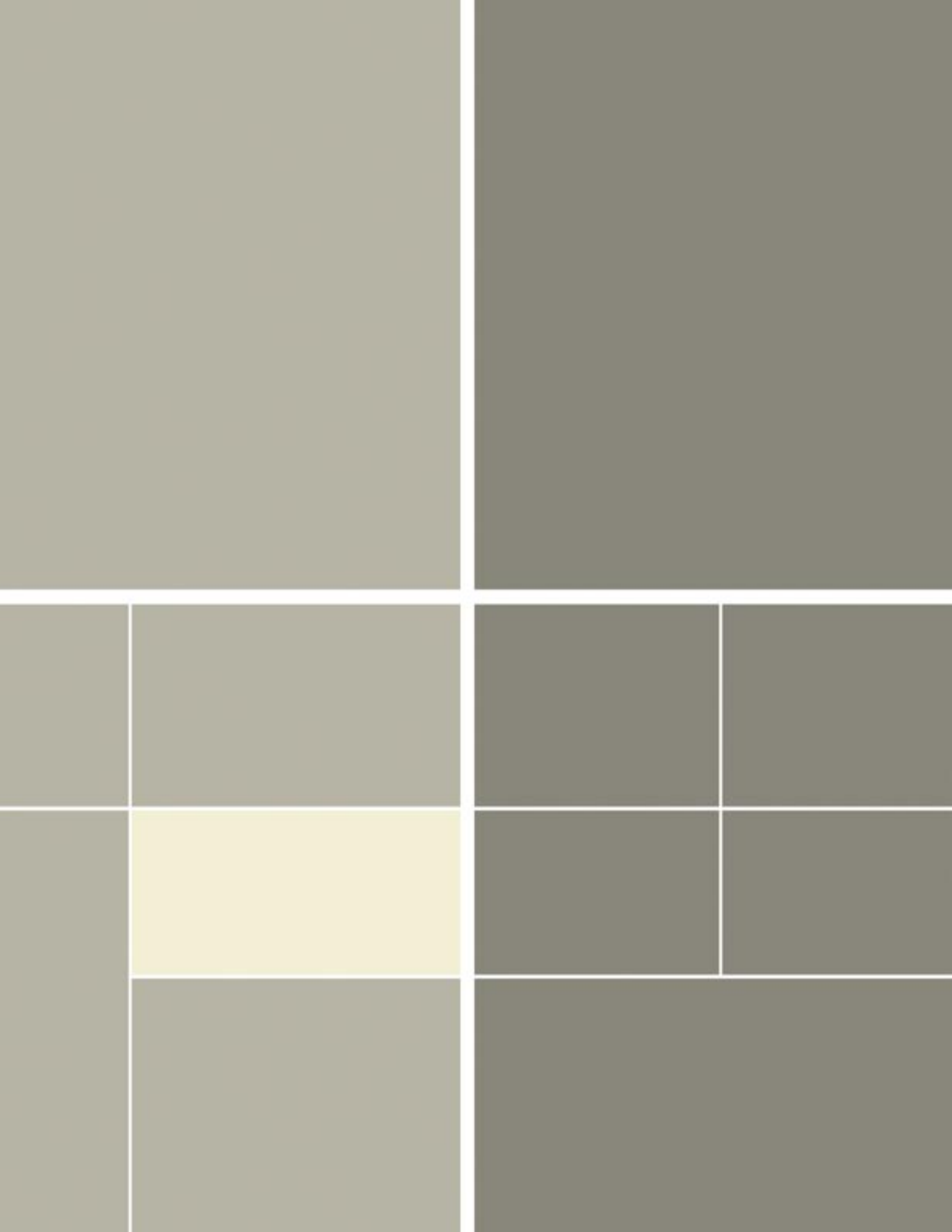


*Biophysics
Research Highlights*





Experimental Studies and Computer Models of the Retina for Visual Prostheses

J. George, G.T. Kenyon, A. Yamauchi, B. Perry, X.-C. Yao, B. Barrows (P-21)
B. Travis (EES-6)

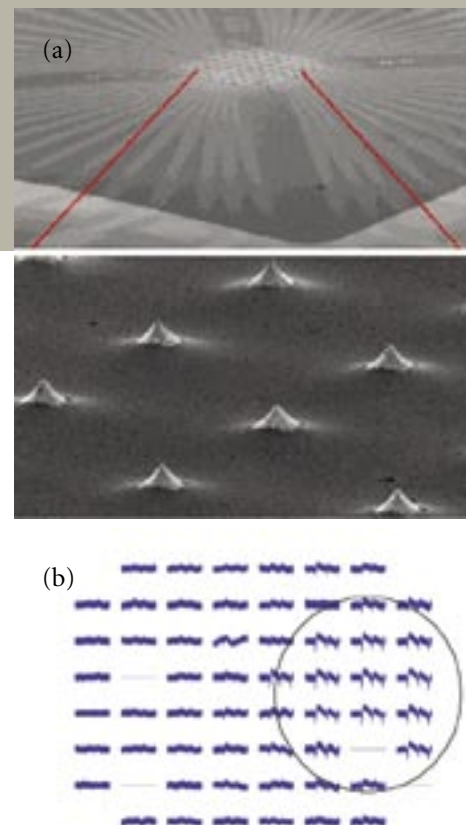


Figure 1. Retinal recordings with a MEA. (a) Scanning electron micrograph of a three-dimensional MEA used for single-unit and local field-potential recordings in an isolated amphibian retina. (b) Spatial pattern of electrophysiological response of an isolated retina to an illumination spot. The retina was placed ganglion cell surface down on a planar MEA. Location of an illumination spot produced by a light-emitting diode is illustrated.

Several common forms of adult-onset blindness are characterized by a massive loss of photoreceptors but a relative sparing of fibers in the optic nerve. In principle, patients suffering from such visual impairments could benefit from a prosthetic system capable of acquiring images, processing and properly encoding the information, and electrically (or magnetically) stimulating remaining retinal neurons. Preliminary studies using a crude prototype of such a device have yielded encouraging results¹, but a number of biomedical, electronic, and neuroscience issues must be addressed before the potential of this technology can be fully realized.

A consortium of DOE laboratories is working on the difficult technical problems that must be solved to achieve a satisfactory “artificial retina.” Los Alamos researchers are developing techniques for imaging patterns of activation within the retina, based on fast optical signals as well as microelectrode arrays (MEAs). These methods will be used to characterize the efficacy of electrical stimulation of the retina and evaluate alternative strategies for stimulation. In order to optimize the processing and encoding of visual information to drive a retinal prosthetic implant, we hope to discover and characterize important aspects of information processing performed by the visual system by coupling dynamic functional imaging techniques with detailed computational simulations of networks. Understanding how the retina encodes visual information is critical for achieving maximum benefit from a prosthetic device and may suggest new image-processing strategies for computer vision systems.

Retina Physiology

Electrophysiological measurements are the gold standard for characterization of neural function, allowing resolution of individual action potentials (spikes) from identified neurons. Multielectrode techniques increasingly allow studies of encoding strategies employed by entire populations of cells², but the measurements are limited by coarse sampling and crosstalk due to tissue conductivity and are disrupted (at least transiently) by electrical stimulation. We have developed functional optical imaging techniques based on measurements of intrinsic optical responses of neural tissue that are closely coupled to electrophysiological activity. However, the signals are tiny; a great deal of work has gone into enhancing size and quality of the responses.

We have undertaken studies of responses to both light and electrical stimulation in isolated amphibian retina (frog or tiger salamander). Electrophysiological recordings have been obtained with single microelectrodes and, more routinely, with MEAs fabricated on a glass substrate that serves as the bottom of the recording chamber. These MEAs consist of 60 metal electrodes in a rectangular array covering several square millimeters of area. The electrodes are connected via

insulated conductors to a multichannel amplifier and data-acquisition system. In some arrays, the electrodes are flat pads. In other commercially available arrays, the electrodes are 40 mm cones rising 70 mm off the array substrate [Figure 1(a)]. We have obtained patterns

RESEARCH HIGHLIGHT PHYSICS DIVISION

Biophysics Research Highlights

of electrophysiological responses reflecting the spatial distribution of the stimulating light using planar MEAs [Figure 1(b)]. With improved experimental technique and using the three-dimensional electrode array, we have been able to regularly record the electroretinogram (the integrated electrophysiological response of the entire retina) as well as local field potential responses with embedded multiunit spike activity (Figure 2). Spikes are extracted from other signal components using digital signal-processing techniques. In the local field potentials (and in single-unit data), we observed a strong oscillatory response (about 30 Hz in frog retina) that was often apparent in single-pass data. These responses are most strongly associated with off responses, i.e., responses to a decrement in illumination, and are most prominent with wide-field stimuli. Responses appear somewhat phase locked to the stimulus, i.e., peaks in the oscillating response waveform appear at about the same point in time relative to the onset or offset of the light stimulus. Signal averaging produced small reductions in the amplitude of the oscillations but did not eliminate them. The reductions were most prominent in the first few cycles of the oscillation, suggesting that the stimulus might reset some ongoing oscillatory driver.

In experiments with a photodiode and video detectors, we have demonstrated

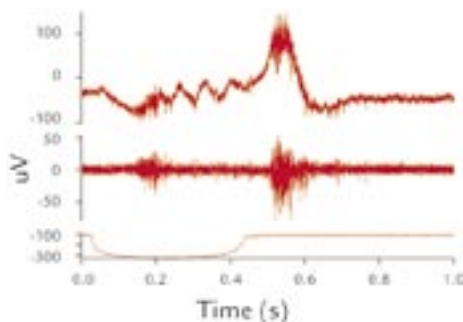


Figure 2. Electrophysiological response of isolated retina to light offset and onset. Upper trace: Single-pass record from one electrode of the MEA. Note the oscillatory off response and embedded spikes. Middle trace: High-pass filtered version of the upper trace showing spiking responses to light onset and offset. Lower trace: Photodiode record of stimulus

that fast intrinsic optical responses can be measured in response to physiological activation of neural circuits including retina (Figure 3), but the signals are very small.³ Unlike other experimental techniques that employ dyes to indicate changes in cellular ion concentration or membrane potential, our methods do not require delivery of chemical to the tissue, so that in principle such measurements can be made noninvasively in the intact human eye. Unlike intrinsic signal imaging based on changes in blood flow or tissue oxygen, we detect changes in tissue light scattering or birefringence that are tightly coupled to the electrical response dynamics of the neurons. With improvements in optical configuration, we have achieved 20-fold increases in signal-to-noise ratio, and recent work has identified other possible improvements. We recently obtained the first dynamic images of the spatial patterns of physiological activation in the retina using these fast intrinsic optical responses. However, because of the small size of the scattering response, we continue to work on improving the image quality. To demonstrate the feasibility of using optical responses to monitor the efficacy of electrical stimulation, we have recently begun a series of experiments to stimulate and record from the retina using a three-dimensional MEA, while simultaneously recording the functional scattered light

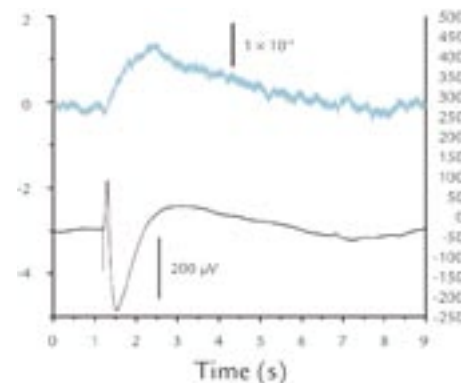


Figure 3. Intrinsic optical response of retina to light stimulation. The retina was placed on an MEA for electrophysiological recording and illuminated with near infrared light in a transmission configuration. Responses are an average of 100 trials. The optical response (upper trace) resembles an integral of the lower electrophysiological response.

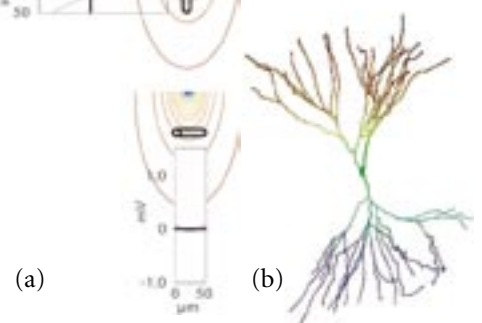
response elicited by stimulation. We have obtained convincing responses in several experiments, with close agreement between the duration of the plateau phase of the response in the optical signal and the corresponding electrophysiological responses recorded across a number of electrodes in the MEA. Optical measures may prove a particularly useful tool for clinical assessment of the retina. We have recently demonstrated that functional responses from retina can be recorded with optical coherence tomography⁴, a technique used routinely to assess retinal anatomy.

The availability of high-density neurophysiological data from this project provides new impetus for linking computational models of neural networks with experimental responses. If we can validate computational methods at the level of retinal neuronal networks, we increase confidence in the feasibility of modeling the dynamics of extended networks within the brain accessible by noninvasive methods.

Modeling Stimulation by a Retinal Prosthesis

An initial objective of computer modeling is to capture the biophysics of

Figure 4. Effects of geometry on electrical stimulation. (a) Change in “membrane potential” along a 50 mm passive cable in response to a 1 mA current. A vertically oriented segment experiences a maximum depolarization of nearly 1 mV at the proximal tip, while a horizontally oriented segment is virtually unaffected by the stimulus. Cable centers were 75 mm from the electrode. (b) Geometrical model of a neuron derived by tracing a labeled cell in the retina.



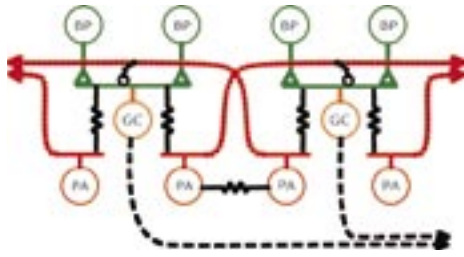


Figure 5. Computational model of retinal circuitry. The full model contained five cell types: bipolar (BP) cells; small, large, and polyaxonal amacrine (PA) cells; and alpha ganglion cells (GC) arranged as a 32×32 square mosaic. Light stimuli were implemented by injecting currents directly into BP cells. Only those elements directly responsible for synchronous oscillations are depicted. A combination of local excitation via gap junctions and long-range inhibition via axon-bearing amacrine cells produced physiologically realistic oscillations. Explanation of symbols: Excitation (triangles), inhibition (circles), and gap junctions (resistors).

electromagnetic stimulation of neural tissue. Neural processes are activated by “gradients” in the extracellular potential and are largely insensitive to the average magnitude, or “direct current offset.” The efficacy of stimulation depends on the design of the electrode array, the properties of the tissue, and the location and orientation of neural processes within the potential field. We have developed a simplified model of the gross anatomy of the retina, and associated structures including the vitreous, retina, and peripheral tissues, as well as the MEA itself. Prosthetic stimulation is modeled by first calculating the extracellular potentials produced by the applied currents and then computing how the resulting gradients act upon dendritic and axonal processes within the retina.

Currents passed through a single isolated electrode produce a dipole-like potential field that is nearly mirror symmetric. The addition of a large insulator (corresponding to a prosthetic device affixed to the vitreous surface) forces more of the current into the retina, enhancing the potential gradient within the tissue and thus the effects of prosthetic stimulation. Our results illustrate that the size of electrodes and the overall design

of the prosthetic device itself, can have a large impact on the spatial distribution of applied currents. After computing the potential distribution within the tissue, we introduce a passive cable segment to simulate the interaction between the tissue electric field and the dendritic structure of the neuron. This allows us to evaluate effects of applied currents on cellular membrane potential and thus for stimulation. Representative results are summarized in Figure 4(a).

This sort of study suggests that our ability to stimulate a particular retinal neuron will depend strongly on the details of the complicated microgeometry of the cell, as well as the spatial distribution of ionic channels within the cell. Our network-simulation software provides an adequate framework to model these functional details. We have recently added capabilities to import geometrical descriptions of real (or virtual) cells [Figure 4(b)], in order to assess the consequences of cellular geometry on the specificity of stimulation by a given configuration of stimulating electrodes. However, the sensitivity of cells to stimulation also depends on the interaction of cells within extended circuits and networks within the retina.

Computer Model of Retinal Coding and Oscillations

The retina consists of several layers of specialized neurons at the back of the eye that collectively perform the transduction and preprocessing of visual signals. The output neurons of the retina, ganglion cells whose axons make up the optic nerve, line the innermost surface of the retina (i.e., closest to the incoming light). In the absence of stimulation, most ganglion cells fire spikes in a random fashion at a background rate much lower than their maximum firing frequency. When stimulated, the firing rate increases markedly in proportion to the local contrast. This modulation of neuronal firing rate by stimulus properties and related observations are the basis for the “rate code hypothesis,” which posits that information is transmitted by the mean number of spikes per unit time irrespective

of their precise timing. Other evidence, however, that the rate code hypothesis is incomplete is that as the size of a visual feature (e.g., a light or dark spot) increases, the total number of spikes is reduced, but a distinct oscillation is often observed in the firing rate. The phase of the oscillation drifts randomly over time so that the responses evoked by separate spots will rapidly become uncorrelated. Remarkably, when a single large spot stimulates two groups of neurons, their oscillations become strongly phase locked, suggesting that the relative timing of spikes in the optic nerve may convey information about the connectedness of visual features.

To study the consequences of interconnections within the retinal circuitry and to explore mechanisms of processing and encoding, we constructed a computer model (Figure 5). The model accounts for responses of certain retinal neurons to temporally modulated stimuli. The temporal modulation transfer function (tMTF) measures how strongly the output of a system is modulated as a function of the frequency of a sinusoidal input. The model retina exhibited a sharp resonance peak in its tMTFs above 60 Hz at frequencies corresponding to experimentally observed oscillatory responses (Figure 6).^{5,6} The model accounts not only for the resonance frequency, but also for an associated kink in the phase response curve that plots how much the phase of the output modulation is shifted relative to the sinusoidal input. Using our computer model, we were able to show that the kink in the phase response curve obtained from retinal ganglion cells was due to entrainment. By exploiting such resonances, we may be able to selectively activate certain retinal neurons at their favored stimulation frequencies.

To assess stimulus-evoked oscillations in the retinal model, we analyzed the local field potentials directly and also considered correlations computed between spike trains from all pairs of ganglion cells activated by the stimulus. The results were combined into an averaged correlation measure. In both the cat retina and retinal model^{7,8}, the phases of the oscillations to

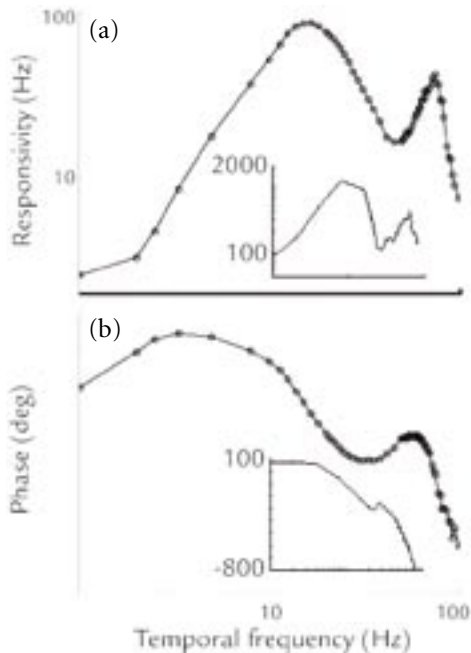


Figure 6. High-frequency resonance in a retinal model. (a) Multiunit tMTF recorded from model ganglion cells. Inset: Similar features were present in the tMTF recorded from a cat alpha ganglion cell in response to a diffuse grating. (b) The response phase plotted as a function of temporal modulation frequency. Inset: The phase-response curve of the cat alpha cell shows qualitatively similar behavior.

small stimuli drift randomly over time so that firing activity becomes uncorrelated over sufficiently long delays. This is a fundamentally nonlinear phenomenon arising from the threshold nature of spike generation; the phase of a linear harmonic oscillator, on average, always remains fixed relative to the stimulus onset. The retinal model was able to account for the experimentally observed size dependence of retinal oscillations (Figure 7). In both experimental data and retinal model results, small stimuli evoked little or no oscillatory response, whereas large stimuli evoked very large oscillations.

Conclusion

Evolving experimental techniques allow us to characterize the mechanism of activation of retinal neurons by electrical stimulation and to explore the processing and encoding of information by retinal neural networks. By coupling these neural population measures to computational models, we can build a useful tool for engineering the neural electronic interface, exploring advanced techniques for stimulation and optimizing the electronic systems employed to encode information for processing and interpretation by the brain.

Reference

1. M.S. Humayun *et al.*, "Visual perception in a blind subject with a chronic microelectronic retinal prosthesis," *Vision Research* **43**, 2573–2581 (2003).
2. B.P. Olveczky, S.A. Baccus, and M. Meister, "Segregation of object and background motion in the retina," *Nature* **423**, 401–408 (2003).
3. D.M. Rector *et al.*, "Scattered light imaging in vivo tracks fast and slow processes of neurophysiological activation," *Neuroimage* **14**, 977–994 (2001).
4. X.-C. Yao *et al.*, "Rapid optical coherence tomography and recording functional scattering changes from activated frog retina," *Applied Optics* (In press).
5. G.T. Kenyon *et al.*, "A model of high-frequency oscillatory potentials in retinal ganglion cells," *Visual Neuroscience* **20**, 465–480 (2003).
6. L.J. Frishman *et al.*, "Spatiotemporal frequency responses of cat retinal ganglion cells," *Journal of General Physiology* **89**, 599–628 (1987).

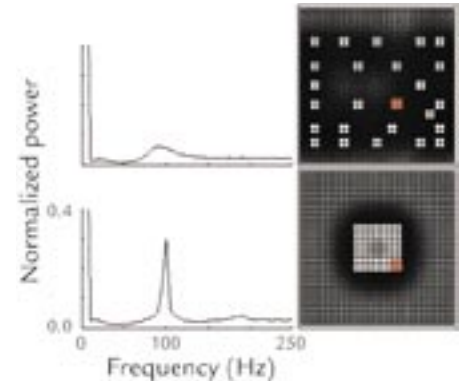


Figure 7. Size dependence of retinal oscillations. Correlation functions computed between model spike trains exhibit a strong increase in oscillatory activity as a function of increasing stimulus size, even when the total area of illumination remains constant. A similar size-dependence was apparent in retinal responses measured experimentally.

7. S. Neuenschwander and W. Singer, "Long-range synchronization of oscillatory light responses in the cat retina and lateral geniculate nucleus," *Nature* **379**, 728–732 (1996).
8. G.T. Kenyon *et al.*, "Stimulus-specific oscillations in a retinal model," *IEEE Transactions on Neural Networks: Special Issue on Temporal Coding for Neural Information Processing* **15**, 1083–1091 (2004).

Acknowledgments

This work has received previous support from LANL Laboratory-Directed Research and Development, National Institutes of Health, and is presently supported by the U.S. DOE as part of the Artificial Retina Consortium.

For further information, contact John George, 505-665-2550, jsg@lanl.gov or Garrett Kenyon, 505-667-1900, gkenyon@lanl.gov.

Ultra-Low-Field Nuclear Magnetic Resonance and Magnetic Resonance Imaging

A.N. Matlachov, P.L. Volegov, M.A. Espy, J.C. Mosher, J.S. George, R.H. Kraus, Jr. (P-21)

A primary thrust in clinical nuclear magnetic resonance (NMR) spectroscopy and magnetic resonance imaging (MRI) has been towards ever-higher magnetic-field strengths. For example, clinical images increasingly are moving from 1.5 T to 3–4 T and research instruments for humans are operating at 7 T or higher. This is largely motivated by the enhanced sensitivity at high fields due to increased polarization and increasing detection efficiency at higher frequencies.

Nevertheless, very low field (VLF, in the mT range) and ultra-low-field (ULF, in the μ T range) NMR and MRI are areas of active interest. Cost and size of systems could be significantly reduced. VLF and ULF systems could be easily portable and the sample need not be restricted to the interior of a magnet bore (*ex situ* or “inside out” imaging). Other interests are driven by the complications of using high-field MRI with samples containing metal (i.e., subjects with metal pins or implants), which are minimized at low fields. Furthermore, we recently demonstrated that samples contained entirely inside metallic shells may also be imaged at ULF.¹

Measurement fields do not have to be highly homogeneous to achieve narrow NMR line widths at ULF. Moreover, for a fixed relative homogeneity, the NMR line width scales linearly with the strength of the measurement field, allowing the possibility of very narrow NMR lines with high signal-to-noise at ULF.² Susceptibility artifacts caused by coupling between the applied magnetic field and different sample materials broaden resonance lines

at high fields but are significantly reduced at ULF. The absence of such artifacts may provide opportunities for novel forms of functional imaging at ULF. For example, it may be possible to manipulate T_1 (longitudinal relaxation time of the spin polarization) contrast at low field strength to provide significant contrast not realizable at high fields.

SQUIDS and Magnetic Scanning

NMR spectroscopy detects the magnetic signature of nuclear spins precessing in the measurement magnetic field. At low field strength, signals become increasingly difficult to measure with conventional detectors. Superconducting quantum interference devices (SQUIDS) are magnetic-flux-to-voltage converters of exquisite sensitivity with a response that is independent of frequency. For this reason, a number of low-field NMR systems have employed SQUID sensors at measurement fields below 10 mT, using both high- T_c (liquid-nitrogen cooled) and low- T_c (liquid-helium cooled) SQUIDS. Low- T_c SQUIDS provide higher sensitivity (due primarily to lower thermal noise) and greater reliability and robustness than presently available in high- T_c devices.

The frequency-independent response of SQUID detectors also enables one to simultaneously detect the signature from

multiple different nuclei, even though their NMR frequencies can differ by factors of 2 or more.³ We have recently demonstrated this in our own system as well.⁴ Various investigators, including ourselves, have already demonstrated that ULF MRI is possible (see for example, References 1, 3, and 5). In addition, we recently completed the first-ever demonstration of the feasibility of magnetic resonance (MR) measurements with simultaneous recordings of biomagnetic signals from the brain (magnetoencephalography, MEG), heart (magnetocardiography, MCG) and muscle (magnetomyography, MMG), using the same detectors.^{1,4,6,7}

SQUID-based biomagnetic measurements are noninvasive techniques that measure magnetic fields outside the body, for example at the surface of the head in MEG. These fields arise as a direct consequence of electrical activity (neurons or nerves) in the living body. MEG requires the use of SQUID sensors to measure the extraordinarily low-level magnetic fields, usually in the range from 10^{-15} to 10^{-12} T, produced by neuronal activity in the brain. While other functional imaging modalities, such as functional MRI, depend on the relatively slow and indirect hemodynamic response of the brain, MEG (and electroencephalography, or EEG) can provide measurement of the electromagnetic fields arising

RESEARCH HIGHLIGHT

PHYSICS DIVISION



Biophysics Research Highlights

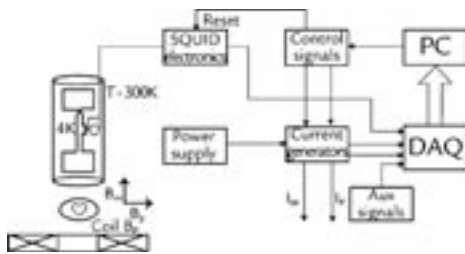


Figure 1. Schematic diagram of the system used to measure simultaneous NMR and biomagnetic signals. Current generators provide current to the magnetic field coils producing B_p and B_m . Control signals allow the computer (PC) to adjust SQUID settings and current levels. AUX signals are auxiliary signals acquired by the data acquisition (DAQ) such as trigger signals, ECG data, etc.

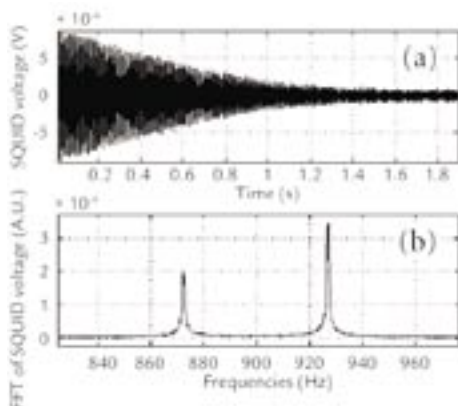


Figure 2. (a) FID for both H_2O and $C_{10}F_{18}$. (b) The FFT of the data in (a) showing the peaks from fluorine (~ 872 Hz) and protons (~ 927 Hz). Data for both solutions were taken simultaneously.

from the actual neuronal currents with submillisecond temporal resolution. Acquiring MR and biomagnetic data simultaneously will reduce most of the sources of error in colocalization of bioelectric sources with anatomy. This will be particularly valuable for MEG and EEG where data typically must be superimposed on conventionally acquired MRI images, introducing significant error.

Perhaps the most compelling application of NMR/MRI at ULF is to acquire direct evidence of biomagnetic signals with a tomographic imaging modality. Specifically, it is speculated that the

bioelectric currents that produce the signals we measure in MEG, MCG, or MMG may produce changes in the proton precession signal, in either frequency, phase, T_2^* (total relaxation time of the spin polarization), etc. If such a signature could be detected, it would allow one to tomographically localize the effect of those currents using MR techniques, thereby eliminating the complications of the inverse problem inherent in biomagnetic source localization. Our team has recently begun investigating this phenomenon.^{4,7}

Measurements of ULF NMR and MRI

Figure 1 shows a schematic diagram of the ULF NMR system designed in Biological and Quantum Physics (P-21). This configuration uses a tangential gradiometer and is optimized for the measurement of simultaneous measurements of MCG and NMR.⁴ Figure 2 shows the free induction decay (FID, the actual signal of spin precession) from a sample of H_2O and $C_{10}F_{18}$ taken simultaneously, and a fast Fourier transform (FFT) of the signal.⁴ As noted previously, this would not be possible with a conventional MR system, as the receiver coils would not be able to detect two frequencies so far apart. An example of the utility of such measurements is to food science, where conventional high-field NMR has already become a powerful tool for the detection of moisture content, sugar content, adulteration, bacterial spoilage, etc.⁸ Our methods suggest a strategy for inspecting food inside metallic cans. We measured the hydrogen-1 NMR signal from tomato juice and cola inside unopened aluminum cans and observed very different T_2^* times: cola ~ 1500 ms, tomato juice ~ 300 ms.

We have also been able to acquire simple images with our system. Figure 3(a) is a photograph of a 60 mm diam by 52 mm high cylindrical plastic phantom with seven 10 mm diam by 48 mm deep wells. Four of the wells were filled with water (shown filled with colored water for visibility). Figure 3(b) illustrates a two-dimensional (2-D) image of the

phantom constructed from a series of gradient-encoded FID spectra acquired at various angles by rotating the sample within a fixed measurement field. The measurement field was $7.8 \mu T$ and the gradient was $\sim 7 \mu T/m$.

Simultaneous Measurements of Biomagnetic Signals and NMR

Figure 4 shows data recorded for our measurement of simultaneous MEG and NMR. The blue trace is the proton FID curve and the red trace is the evoked somatosensory response from a region of human cortex. The stimulus was delivered to the median nerve (thumb) at time $t = 0.1$ s, producing the artifact seen at that time, and the expected N20 response at 20 ms poststimulus and subsequent somatosensory components⁹ are clearly visible. These measurements, combined with the imaging demonstrated in Figure 3, demonstrate that it is possible to combine the advantages of low-field NMR/MRI with high-temporal-resolution MEG measurements. The possibility of imaging simultaneously with biomagnetic recordings could be useful for cardiac diagnostic testing and may alleviate some of the issues surrounding localization of MEG sources relative to anatomy.

The Quest for a Signature or Direct Neuronal Measurements with ULF MR

One very compelling application of NMR/MRI at ULF is to acquire direct evidence of biomagnetic responses producing changes in the proton precession signal, in either frequency, phase, T_2^* , etc. If such a signature could be detected, it would allow one to tomographically localize the effect of those currents using MR techniques, thereby eliminating the complications of the inverse problem inherent in biomagnetic source localization. This would open up a whole new imaging modality.

To study these effects we looked at T_2^* values for NMR signals that were simultaneously acquired in the presence of biomagnetic signals such as those

from heart (MCG) and muscle (MMG). Our hypothesis was that the value of T_2^* in the presence of bioelectric currents would be shorter than that measured when such currents were absent, because inhomogeneity in the local fields should produce a dephasing of spin signals.

Figure 5 shows the simultaneously acquired NMR and MCG data. NMR signals were recorded at various times during the heartbeat, as indicated in the figure. Data for approximately 100 heartbeats were averaged after removing specific noise components (power-line harmonics, cryostat demagnetization signal, and eddy current signal), and filtering.

We focused on the values of T_2^* for NMR during the “T” peak (200–250 ms after the “R” peak) and for NMR during the resting phase of the heartbeat (400–700 ms after the “R” peak). These values were calculated by the direct exponential curve resolution algorithm (DECRA)¹⁰ and the estimated T_2^* was extracted from the damped exponential found at the Larmor (precession) frequency.

T_2^* values varied among subjects with the shortest being 76 ms and the longest being 123 ms. We hypothesize that physiological differences among subjects such as fat content in the chest wall contribute to the spread in values. We observed that the values of T_2^* for the resting phase appeared longer than those for the “T” peak by 2–9 ms for four of the five subjects (as we would expect), however was shorter by 5–7 ms for one subject. Our uncertainty in T_2^* for water phantoms with varying concentrations of copper sulfate was found to be ± 1 ms. However, it is very difficult to estimate the uncertainty in T_2^* for measurements where the sample geometry is so much more complicated and variable.

Because of the complexity of the muscle responses in the cardiac system, we chose to use MMG to investigate the effect of the bioelectric currents on the NMR signal T_2^* . The bioelectric currents during MMG are much larger than neuronal currents, and unlike MCG, effects such as motion,

blood flow, and blood volume of the sample being measured are significantly reduced.

The experiments provide data with interleaved epochs of NMR recorded while the muscles of the forearm were either stressed or relaxed. This protocol was chosen to try and reduce any hemodynamic or metabolic effects. The probability density functions (PDFs) of T_2^* were then inferred from the data for both stressed and relaxed conditions using a “bootstrap” method.⁴ The results are shown in Figure 6. The same analysis approach was then applied to random permutations of the stressed and relaxed sets. The inferred PDF for the randomly mixed data is shown in Figure 7.

The permutation test (Figure 7) shows no inherent preference in our processing between the two sets, while the bootstrap tests (Figure 6) suggest that the two conditions may be distinct, but with statistically low power. Our observed difference in T_2^* for the two conditions is not statistically significant; however, it is encouraging that the trend of a shorter T_2^* for the stressed condition is what one would expect if this effect were due to bioelectric currents dephasing the NMR signal. We caution that even if this effect were statistically significant, we are not yet able to rule out that the measured effect was due to a systematic error due to the slight differences in the experimental configuration between the two cases (i.e., slightly different arm position), some other systematic error in our hardware, or a biological effect that is not electrical in nature.

Discussion and Conclusions

We have demonstrated that biomagnetic signals can be acquired simultaneously with NMR data using SQUID sensors at ultralow magnetic fields. We have demonstrated MRI at these low fields for water phantoms. These results provide the basis of performing MR anatomical imaging simultaneously with bioelectric source localization. Such capability will greatly enhance the efficacy and

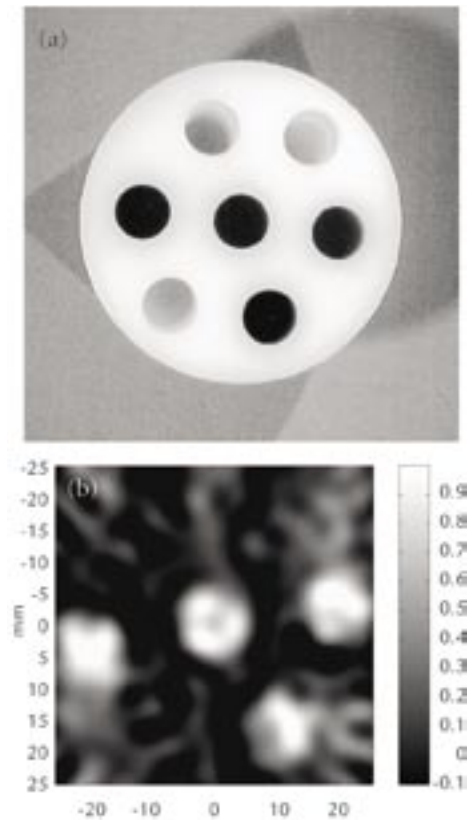


Figure 3. (a) Photograph of a 60 mm diam cylindrical plastic phantom with seven 10 mm diam wells. Four of the wells were filled with water (colored water for visibility). (b) Image of the phantom (2-D) constructed from a series of gradient encoded FID spectra acquired by rotating the sample within a fixed measurement field. The gradient was produced by slightly unbalancing the current in the Helmholtz coils. The average over ~ 100 epochs is shown.

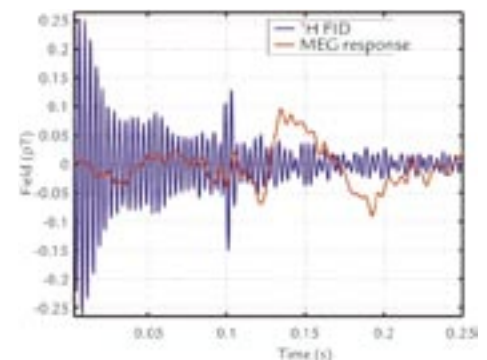


Figure 4. Simultaneous hydrogen-1 NMR FID (blue trace) and MEG somatosensory response (red trace) acquired from a region of the human head including the somatosensory cortex.

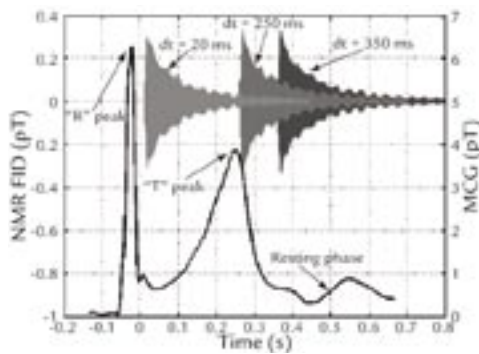


Figure 5. Simultaneously acquired NMR and MCG data. NMR was acquired at the various times indicated during the MCG.

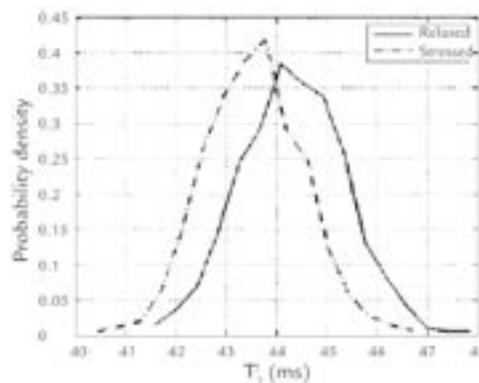


Figure 6. Probability density of T_2^* inferred from 1000 bootstraps for stressed and relaxed epochs.

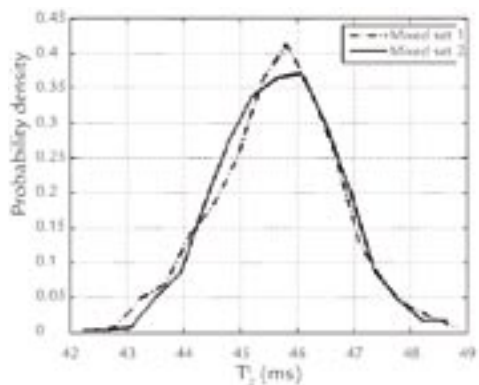


Figure 7. Probability density of T_2^* inferred from the randomly permuted data set.

reduce errors over current functional neuroimaging techniques. In addition, we have investigated the possibility of using MR techniques to tomographically image the direct consequence of bioelectric activity in living tissue. Although there is significant work to be done, we are encouraged that the modality of ULF NMR with SQUIDS is going to be able to see these direct effects and open up a whole new way to gain knowledge regarding bioelectric function.

If nothing else, we have demonstrated that simultaneous anatomical and bioelectric images are possible, and that the field of ULF NMR/MRI with SQUIDS has an exciting future.

References

1. A.N. Matlachov *et al.*, "SQUID detected NMR in microtesla magnetic fields," *Journal of Magnetic Resonance* **170**, 1–7 (2004).
2. R. McDermott *et al.*, "Liquid-state NMR and scalar couplings in microtesla magnetic fields," *Science* **295**, 2247–2249 (2002).
3. R. McDermott *et al.*, "SQUID-detected magnetic resonance imaging in microtesla magnetic fields," *Journal of Low Temperature Physics* **135**, 793–821 (2004).
4. M.A. Espy *et al.*, "SQUID-based simultaneous detection of NMR and biomagnetic signals at ultra-low magnetic fields," *Applied Superconductivity Conference: Harnessing the Magic (ASC'04)*, Jacksonville, Florida, USA, October 3–8, 2004, Los Alamos National Laboratory document LA-UR-04-1544 (accepted for publication in *IEEE Transactions on Applied Superconductivity*).
5. S. Kumar, W.F. Avrin, and B.R. Whitecotton, "NMR of room temperature samples with a flux-locked dc SQUID," *IEEE Transactions on Magnetics* **32**, 5261–5264 (1996).
6. P.L. Volegov *et al.*, "Simultaneous magnetoencephalography and SQUID detected nuclear MR in microtesla magnetic fields," *Magnetic Resonance in Medicine* **52**, 467–470 (2004).
7. M.A. Espy *et al.*, "Simultaneously detected biomagnetic signals and NMR," 14th International Conference on Biomagnetism (BIOMAG 2004), Boston, Massachusetts, USA, August 8–12, 2004, Los Alamos National Laboratory document LA-UR-04-6823.
8. I.L. Pykett, "NMR—a powerful tool for industrial process control and quality assurance," *IEEE Transactions on Applied Superconductivity* **10**, 721–723 (2000).
9. C.C. Wood *et al.*, "Electrical sources in human somatosensory cortex: Identification by combined magnetic and potential recordings," *Science* **227**, 1051–1053 (1985).
10. A. Nordon *et al.*, "Quantitative analysis of low-field NMR signals in the time domain," *Analytical Chemistry* **73**, 4286–4294 (2001).

Acknowledgment

The authors wish to thank Dr. C.C. Wood for his thoughtful discussions of the topics presented. Technical development of the instrumentation used for this work was supported by LANL and the Defense Advanced Research Projects Agency. Experimental studies received support from the U.S. DOE Office of Biological and Environmental Research.

For further information, contact Robert Kraus, Jr., 505-665-1938, rkraus@lanl.gov.

Stochastic Closure for Multiscale Simulations

D.M. Schmidt, S.C. Jun (P-21), B. Nadiga, D. Livescu (CCS-2), D. Higdon (D-1), D. Ranken (CCN-12)

In nonlinear systems, small-scale phenomena affect large-scale behavior. Computer simulations of large, nonlinear systems, therefore, require very large grids in order to both cover the domain of the problem and to resolve the finest relevant small-scale phenomenon. Existing computing capabilities are often inadequate to compute on grids that fully resolve the small-scale phenomena resulting in the use of coarser grids. In such cases, the equations governing the dynamics of the system to be simulated must be modified to try to replicate the effects of the now missing, subgrid-scale phenomena. This problem of how to modify the equations to replicate the subgrid phenomena is known as the problem of closure, and any particular modified set of partial differential equations (PDEs) is called a particular choice of closure relation. In practice, generating closure relations is a very problem-specific, time-consuming endeavor, often involving the generation and fine-tuning of models to incorporate phenomenological information and/or theoretical insights about the particular system to be simulated.^{1,2}

Yet another ubiquitous problem associated with simulating complex systems is uncertainty quantification. Input parameters, boundary conditions, and physics-model parameters are often unknown and affect the outcome of the simulation. In order to quantify the uncertainty of the output of the simulation, given that of the input parameters, the simulation must be run many times with different values of the parameters.^{3,4}

The problems of closure and of uncertainty quantification are correlated for a number of reasons. First, closure must be accomplished on a sufficiently coarse grid to allow for multiple runs of the simulation. Second, the act of up-scaling a system of equations to a coarse grid and choosing a closure relation is a source of uncertainty; different closure relations can be used, producing different results.

Our Approach to Closure

We are working to develop, validate, and apply a new probabilistic approach to the problems of closure and uncertainty quantification in multiscale simulations through stochastic closure (SC). Our SC approach uses a probability distribution of closure relations as the solution of the closure problem. This probability distribution represents information about the unresolved phenomena that may be obtained from the output of a simulation on a fine grid that resolves the small-scale phenomena over a smaller domain, as well as from relevant experimental results. Statistical methods for density estimation can be used to generate a distribution that encodes this information. Once the probability distribution is obtained, individual closure relations are drawn at random and used throughout the

evolution of the simulation. Uncertainties in the choice of closure relations are clearly defined and better sampled in this approach. Moreover, the effects of unresolved phenomena tend to be better represented with this SC approach than with the use of a single closure relation. Finally, by addressing the closure issue with generalized probabilistic methods, the tools and technologies that we are developing will be applicable to a range of multiscale systems.

Rationale

The rationale for SC derives from the following considerations. Any coarsely sampled or gridded field could have resulted from one of a large number of different nonsampled, or continuous fields. The different continuous fields generate different dynamics in the nonlinear terms of the dynamical equations, resulting in a large number of different closure relations that could be used. Constructing a probability distribution of closure relations allows one to incorporate information about the likelihood of any particular closure relation based on prior information about the subgrid-scale phenomenon for that dynamical system. This information is contained within the original dynamical equations and may be found by simulating the system over a

RESEARCH HIGHLIGHT
PHYSICS DIVISION

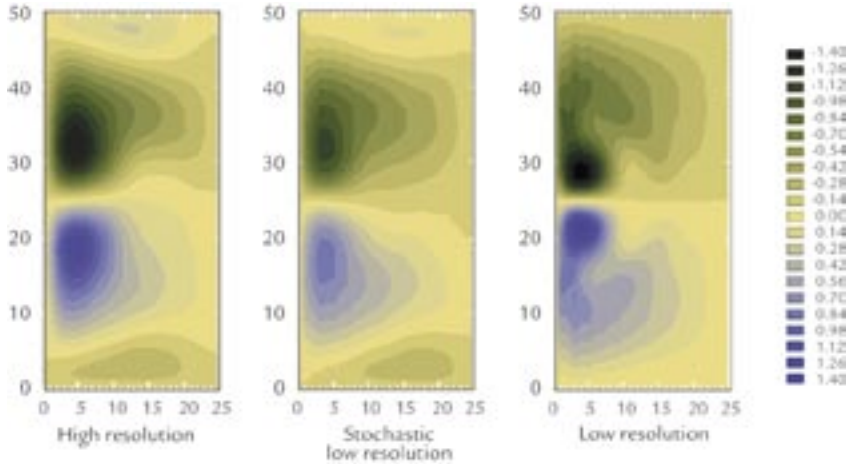


Figure 1. Time-averaged stream function plotted over the two-dimensional domain of the sample problem, resulting from three different simulations. Left panel is from a high-resolution simulation that fully resolves the nonlinear phenomena and represents the “true” results. Right panel resulted from an uncorrected simulation of the same PDEs but on a low-resolution coarse grid. Middle panel resulted from the average of 10 simulations with SC correction on the coarse grid.

small domain with a fine enough grid to resolve the small-scale phenomenon.

If successfully utilized, a number of potential benefits may result from these ideas. By treating closure as a probabilistic problem where a probability distribution is generated based on the output of a fine-scale simulation, the statistical techniques developed to generate such a distribution can be applied to a wide range of problems and in a nearly automated fashion. This diminishes the historical problem of generating closure relations as being a problem-specific, time-consuming endeavor. By drawing from a distribution of closure relations throughout multiple simulations, the uncertainty associated with up-scaling to a coarse grid are inherently included and in a manner that allows for other uncertainties to be included as well. This significantly aids the uncertainty quantification goal. Moreover, because multiple closure relations are being used, the time average of multiple moments of fields is well reconstructed, not just one or a few moments. Though others have used SC terms⁵, they have been problem specific and have not been formulated in the generalized statistical terms we propose here, nor did they address the important problem of uncertainty quantification.

Example

We have used a simple barotropic model of the subtropical/subpolar gyre (rotating flow) circulation in the ocean as a prototypical multiscale problem to illustrate the SC approach. The time-averaged stream function from a high-

resolution, 200×100 grid simulation shows a pair of inner wind-driven, counter-rotating gyres and a pair of outer gyres (left panel of Figure 1) that are driven by turbulent eddy fluxes.⁶ In a low-resolution 50×25 grid simulation, using the same dynamical equations and identical setting, the time-averaged stream function does not contain the outer pair of eddy-driven gyres and the magnitude of circulation is lower in the inner pair of wind-driven gyres (right panel of Figure 1).

To construct a distribution of closure relations for the low-resolution simulation, we used the results of the high-resolution simulation. The dynamical system involved a single nonlinear term in the PDEs that was a Jacobian of two fields, $J(p, q)$. To construct the SC distribution, we examined the local spatial average (to represent the act of down-sampling to a coarser grid) of the Jacobian versus the Jacobian of the spatially averaged fields. Specifically, we looked at $\langle J(p, q) \rangle$ versus $J(\langle p, q \rangle)$, where $\langle \rangle$ denotes local spatial average. A scatter plot of these quantities from the output of the fine-scale simulation for a local region in the

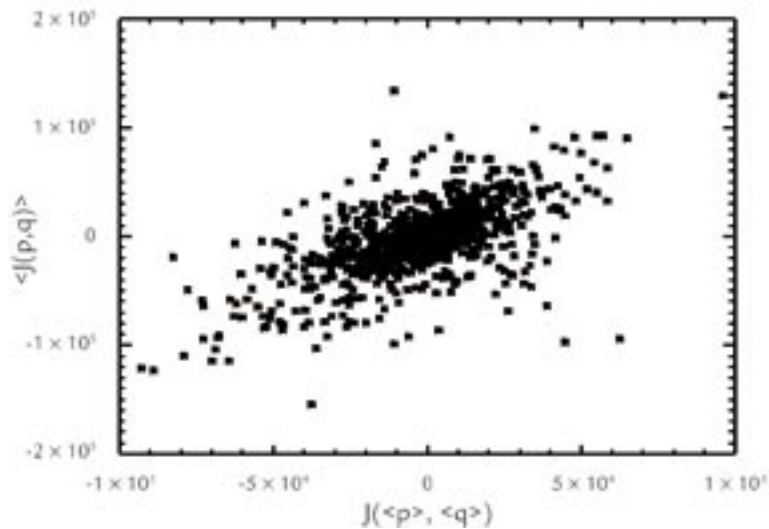


Figure 2. Scatter plot demonstrating the nonlinear Jacobian of the coarsely sampled fields (horizontal axis) versus the coarsely sampled Jacobian of the finely sampled fields (vertical axis). We are given the values on the horizontal axis during the evolution of the PDEs on a coarse field, but the true values of the Jacobian are on the vertical axis. This error is due to the coarse sampling of the fields, and a closure relation is the algorithm used to calculate the correction. Our SC approach samples closure relations from a probability distribution constructed to represent the nondeterministic nature of the closure problem.

two-dimensional spatial domain is shown in Figure 2. When integrating the PDEs on a coarse grid we are given $J(\langle p, q \rangle)$ but would like to know $\langle J(p, q) \rangle$. Clearly, no single choice exists for this but rather a range of choices that we approximate by constructing a distribution (Figure 2).

The low-resolution simulation was rerun, but modified to include a SC term to model the subgrid turbulence that was randomly sampled from the previously found distribution, assuming a temporally homogeneous model for the subgrid phenomena temporal correlation. Adding this sampling step did not significantly add to the run time of the code so that we could run multiple stochastic simulations in much less time than it took for one run of the high-resolution simulation. The middle panel of Figure 1 shows the average over multiple stochastic simulations of the time-averaged stream function. The outer pair of gyres now re-emerges and the magnitude of circulation in the wind-driven pair is improved as well.

We also calculated and compared the temporal variability (standard deviation over time) of the stream function for each type of simulation (Figure 3). The low-resolution run completely failed to reproduce the temporal variability found in the high-resolution run, but the low-resolution stochastic run did a good job in reproducing this variability. These results indicate that multiple moments of the fields are reproduced well with this SC approach. Moreover, the variance or uncertainty of any

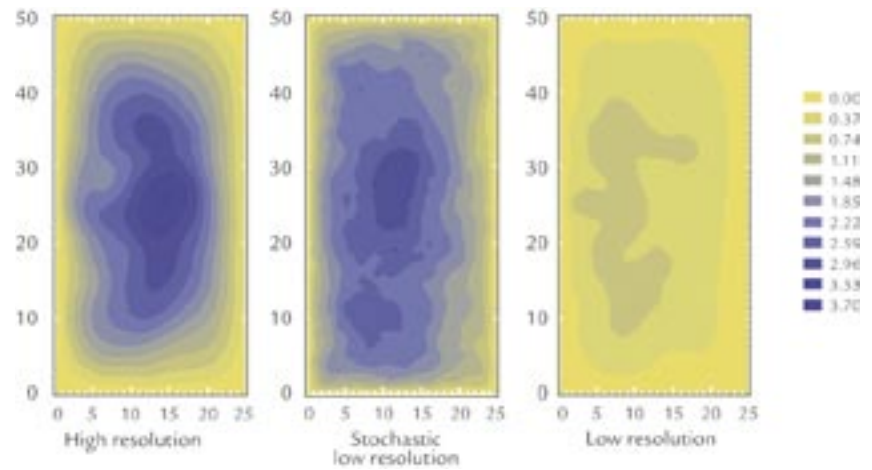


Figure 3. Similar to Figure 1, however, the standard deviation of the stream function over time is shown, rather than the average over time. This shows that multiple moments of the stream function are reproduced well in the SC approach.

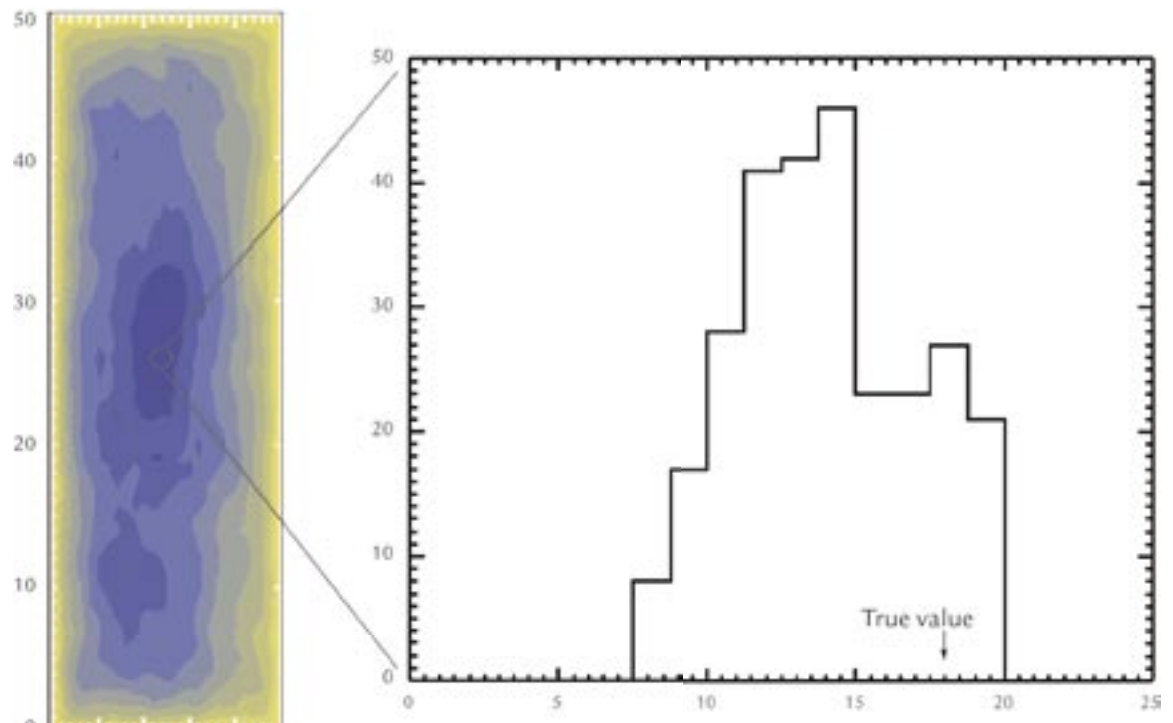


Figure 4. Illustrating how uncertainty is estimated in the SC approach. The left panel is a duplicate of the middle panel of Figure 3, showing the standard deviation over time of the stream function (SDSF) and averaged over multiple SC simulations. The panel on the right shows the histogram of this quantity over the multiple SC simulations for the region shown in the circle on the left panel figure. This histogram represents the relative probability of the SDFS values, which quantifies the uncertainty of this quantity. The true value is shown in the figure and is consistent with this distribution.

Biophysics Research Highlights

quantity may be estimated by simply calculating the variance of that quantity across the multiple stochastic closure runs, as shown in Figure 4.

Conclusion

We are developing a novel method to model the effects of unresolved subgrid phenomena and to quantify uncertainty in simulations of nonlinear PDEs. Our method is based on a probability distribution of closure relations that is sampled and added to each time evolution step of the simulation of the unmodified PDEs. We have demonstrated this approach with a simple two-dimensional ocean model and are working to develop this method so that it can generally be applied to a wide range of problems.

References

1. B.T. Nadiga and L.G. Margolin, "Dispersive eddy parameterization in a barotropic model," *Journal of Physical Oceanography* **31**, 2525–2531 (2001).
2. D.D. Holm, J.E. Marsden, and T.S. Ratiu, "Euler-Poincare models of ideal fluids with nonlinear dispersion," *Physical Review Letters* **80**, 4173–4177 (1998).
3. M.D. McKay, R.J. Beckman, and W.J. Conover, "A comparison of three methods for selecting values of input variables in the analysis of output from a computer code," *Technometrics* **21**, 239–245 (1979).
4. W.J. Welch *et al.*, "Screening, predicting, and computer experiments," *Technometrics* **34**, 15–25 (1992).
5. C.E. Leith, "Stochastic backscatter in a subgrid-scale model: plane shear mixing layer," *Physics of Fluids A* **2**, 297–299 (1990).
6. R.J. Greatbatch and B.T. Nadiga, "Four-gyre circulation in a barotropic model with double-gyre wind forcing," *Journal of Physical Oceanography* **30**, 1461–1471 (2000).

Acknowledgment

This work is supported by the LANL Laboratory-Directed Research and Development program.

For further information, contact David Schmidt, 505-665-3584, dschmidt@lanl.gov.



The World's Greatest Science Protecting America

Los Alamos National Laboratory, an affirmative action/equal opportunity employer, is operated by the University of California for the U.S. Department of Energy under contract W-7405-ENG-36.

